

Effect of conductivity on the electromigration-induced morphological evolution of islands with high symmetries of surface diffusional anisotropy

Cite as: J. Appl. Phys. **129**, 025110 (2021); <https://doi.org/10.1063/5.0033228>

Submitted: 15 October 2020 • Accepted: 23 December 2020 • Published Online: 12 January 2021

 Jay Santoki,  Arnab Mukherjee,  Daniel Schneider, et al.



View Online



Export Citation



CrossMark

ARTICLES YOU MAY BE INTERESTED IN

[Role of conductivity on the electromigration-induced morphological evolution of inclusions in {110}-oriented single crystal metallic thin films](#)

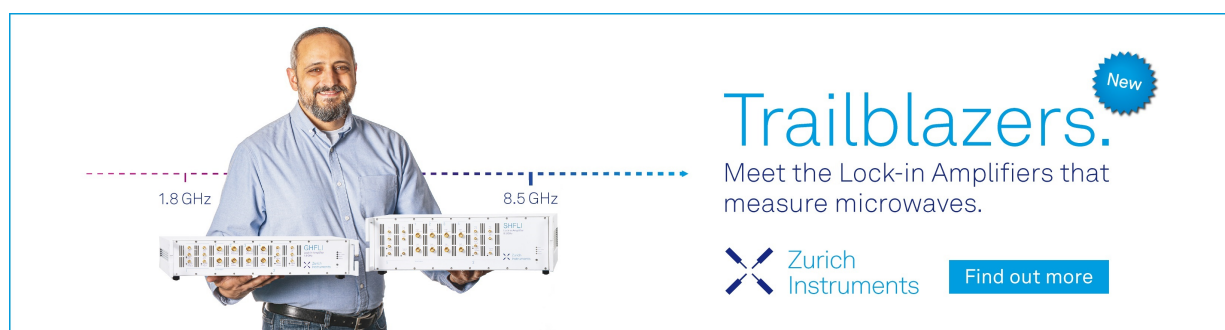
Journal of Applied Physics **126**, 165305 (2019); <https://doi.org/10.1063/1.5119714>

[Phase-field simulations of electromigration-induced defects in interconnects with non-columnar grain microstructure](#)

Journal of Applied Physics **127**, 175301 (2020); <https://doi.org/10.1063/1.5145104>

[Free Energy of a Nonuniform System. I. Interfacial Free Energy](#)

The Journal of Chemical Physics **28**, 258 (1958); <https://doi.org/10.1063/1.1744102>



Trailblazers. 

Meet the Lock-in Amplifiers that measure microwaves.

 Zurich Instruments [Find out more](#)

Effect of conductivity on the electromigration-induced morphological evolution of islands with high symmetries of surface diffusional anisotropy

Cite as: J. Appl. Phys. 129, 025110 (2021); doi: 10.1063/5.0033228

Submitted: 15 October 2020 · Accepted: 23 December 2020 ·

Published Online: 12 January 2021



View Online



Export Citation



CrossMark

Jay Santoki,^{1,a)} Arnab Mukherjee,² Daniel Schneider,^{1,3} and Britta Nestler^{1,3}

AFFILIATIONS

¹Institute of Applied Materials (IAM-CMS), Karlsruhe Institute of Technology (KIT), Strasse am Forum 7, 76131 Karlsruhe, Germany

²Center for Hierarchical Materials Design (CHiMaD), Northwestern University, 2205 Tech Drive, Evanston, Illinois 60208, USA

³Institute of Digital Materials Science (IDM), Karlsruhe University of Applied Sciences, Moltkestrasse 30, 76133 Karlsruhe, Germany

^{a)}Author to whom correspondence should be addressed: santoki@kit.edu

ABSTRACT

We report on the electromigration-induced morphological evolution of islands (vacancies, precipitates, and homoepitaxial adatom clusters) using a phase-field method with high symmetries of surface diffusional anisotropy. The analysis emphasizes on islands migrating in the {100} and {111} planes of the face-centered-cubic crystal, which resembles fourfold and sixfold symmetries, respectively. The numerical results intend to elaborate on the role of conductivity contrast between the island and the matrix and the misorientation of the fast diffusion direction with respect to the applied electric field on the morphological evolution. Based on numerical results, a morphological diagram is constructed in the plane of misorientation angle and conductivity contrast delineating a rich variety of morphologies, which includes steady-state, time-periodic, zigzag oscillations, and island breakup. While the shape of the island is primarily dictated by the conductivity contrast, the migration modes depend on the misorientation. The various migration modes are further distinguished based on the shape of the island such as a faceted wedge or seahorse morphology, an oscillatory characteristic such as standing wave or traveling wave time-periodic oscillations, and different breakup features. The steady-state kinetics obtained from the fourfold and sixfold symmetries are critically compared with the twofold symmetry, isotropic analytical, and numerical findings. Our result suggests that the steady-state velocity decreases with the symmetry fold of the island. Furthermore, the influence of variation in conductivity contrast and misorientation on kinetics in the time-periodic oscillations are discussed. Finally, the numerically obtained stable facets are compared with the analytically derived orientations. The observed results have direct repercussions in terms of the fabrication of nanopatterns and the performance of thin-film interconnects.

Published under license by AIP Publishing. <https://doi.org/10.1063/5.0033228>

I. INTRODUCTION

There has been a long-standing interest in understanding and tuning structures at mesoscale and nanoscale by an application of external fields such as mechanical,¹ thermal,^{2,3} magnetic,⁴ and electric field.^{5,6} The electric field, in particular, manifests as a promising choice for guiding pattern formation because of the ease with which it can be applied.⁷ Furthermore, since the electric field scales inversely with the system size,⁸ it is suitable for application in the nanoscale regime. As a result, the electric field as an external guiding agent is fast gaining popularity in directed assembly across a number of material systems such as block co-polymers,^{9,10} fluids,¹¹ liquid metals,¹² and metallic conductors,¹³ among others.

Electromigration-induced atomic motion on the surface of islands (via surface diffusion) such as vacancies, precipitates, and adatom clusters leads to fascinating morphological transitions. Gaining insights into the topological changes in the island shape is critical to ascertain the reliability and successful performance of the interconnect.¹⁴ For instance, void elongation in the transverse direction (with respect to the line) can prove fatal by severing the line and compromising the electrical conductivity.¹⁵ On the other hand, precipitates are purposely added to conductor lines to enhance the lifetime through coarsening and grain-boundary precipitate interaction.¹⁶ For instance, a small number of precipitates of Cu are known to improve the reliability of Al interconnects.¹⁷

Contrary to the menace in metallic lines, electromigration in single layer islands and vacancy clusters (on conducting substrates) provides a new paradigm of the fabrication of nanostructures of desired feature and size.^{7,18,19} In the present article, a general terminology “island” is employed henceforth to refer to vacancies, precipitates, and adatom clusters alike.

Electromigration-induced motion of islands has been modeled previously using analytical and numerical methods. Analytical studies, employing linear stability analysis, focus on the conditions leading to the onset of shape bifurcation of the circular island.^{20–23} No information whatsoever on morphology beyond the bifurcation point, however, can be ascertained.²² The topological evolution of islands has been studied numerically via Monte Carlo and sharp-interface-based continuum theory.^{24–32} Numerical studies provide valuable insights into the many complex transition after bifurcation such as splitting,²¹ coalescence,³⁰ coarsening,¹⁶ faceting,^{31,32} multiple island interaction,²⁷ nanowire formation,²⁸ and oscillatory dynamics.²⁹

While most of the previous works have studied the effect of various parameters such as electric force to capillary force χ ,^{26,33} linewidth to island radius ratio Λ ,³⁴ diffusivity parameters such as anisotropic strength A ,²⁶ grain symmetry m ,^{29,35} and misorientation angle ϖ ,²⁹ the parameter that has perhaps received the least attention is the conductivity ratio between the island and the matrix β . Understanding the role of conductivity contrast is of practical interest.³⁶ A careful consideration of the conductivity contrast is essential to distinguish the contribution of bulk and surface electromigration. In conductor lines, conducting species might be trapped inside the voids leading to finite conductivity. The stability of a circular island with the strength of the electric field was derived using the linear stability analyses.^{20,22} Furthermore, Li and Chen²³ obtained an expression for the elliptical island and compared the kinetics with the circular one.

The main bottleneck in addressing the role of conductivity in the analytical theory is that the solution of the Laplace equation is non-trivial for arbitrary shape, and hence, studies so far have been restricted only to certain geometries such as circular or elliptical.^{20–23} In the front-tracking numerical models, the electric field on the island surface is approximated by the surface projection of the local field taken to be a constant, and the explicit dependence of the electric field on conductivities is not considered.^{29,37} While for larger Λ such a choice might be reasonable, but smaller Λ manifest in a non-local problem due to the coupling of the island shape and electric field thereby leading to the current crowding effect.³⁴

The aforementioned limitations can be circumvented by employing a diffuse-interface model where the kinetic equation of the indicator variable of the two phases known as the phase-field is coupled to a Laplace equation. A general framework can be obtained, which is equally applicable to voids and precipitates in interconnect lines as well as tuning patterns in single layer islands. While the phase-field literature employed for the electromigration-driven island morphology is ample,^{34,38–52} there are only a few works focused on conductivity contrast. For instance, Morgan and Jin³⁸ accounted the effect of anisotropic conductivity on island migration in different grains of the polycrystalline structure. In addition, Li *et al.*³⁹ studied the effect on the stability of the elliptical island and further

highlighted the morphological evolution of crack and wedge-shaped islands influenced by various conductivity contrasts. The present article is an extension of our previous work in Ref. 40, where the island dynamics for a twofold diffusional anisotropy were analyzed. In the present article, the morphological evolution of the higher-order (fourfold and sixfold) symmetrical islands is considered. The aim of the present work is as follows: (i) to investigate the various migration mode in the $\beta - \varpi$ space and (ii) to critically compare the results obtained by fourfold and sixfold symmetrical islands with those of isotropic and twofold islands. The present article is organized as follows: Section II briefly describes the phase-field model to investigate island motion under electromigration. Next, various modes of migration are identified by systematic numerical investigations on fourfold and sixfold symmetrical islands with highlighting underlying mechanisms in Sec. III. In addition, these migration modes are further recategorized by analyzing specific features of morphological evolution. Afterward, Sec. IV briefly discusses on the technological relevance of the numerical results. Finally, Sec. V concludes the article with future guideline.

II. MODEL

For the perception of the presented results, we briefly describe the model. However, a complete description of the model can be found in Ref. 40. An indicator parameter c is introduced to differentiate between the island ($c = 1$) and the matrix ($c = 0$) that are separated by a thin region of finite thickness across which c varies smoothly between the two values. In electromigration-driven island migration, the morphological changes are governed by the relative intensity of the capillary force and the electromigration force. The interaction of these forces can be expressed by a modified Cahn–Hilliard equation as

$$\frac{\partial c}{\partial t} = \nabla \cdot (M(c)\nabla\mu) + \nabla \cdot (M(c)q_s\nabla\phi), \quad (1)$$

where t denotes time, μ is the potential associated with capillarity, q_s is the effective surface charge, and ϕ is the electrical potential whose distribution is derived from the Laplace equation,

$$\nabla \cdot [\sigma(c)\nabla\phi] = 0, \quad (2)$$

where $\sigma(c)$ is the electrical conductivity that is interpolated between the island (σ_{icl}) and the matrix (σ_{mat}). The mobility function is defined as $M(c) = M_{s,max}f(\theta)c^2(1-c)^2$, where $M_{s,max}$ represents maximum adatom mobility of a specific orientation, and the anisotropy function is described as $f(\theta) = (1 + A(\cos^2(m(\theta + \varpi))))/(1 + A)$, where A is the strength of anisotropy, m denotes the grain symmetry parameter, θ represents the local tangent angle, and ϖ is the misorientation angle. A schematic representation of the island with the meaning of various parameters is shown in Fig. 1. The evolution Eq. (1) is normalized for computational convenience with a length scale $\lambda' = 21$ nm and a time scale $\tau' = \lambda'^4 k_B T / (\gamma_s \Omega D_s \delta_s)$, where k_B denotes the Boltzmann constant, T represents the absolute temperature, γ_s is the surface energy, Ω represents the atomic volume, D_s denotes the surface diffusivity, and δ_s is the thickness of the surface layer.³⁴

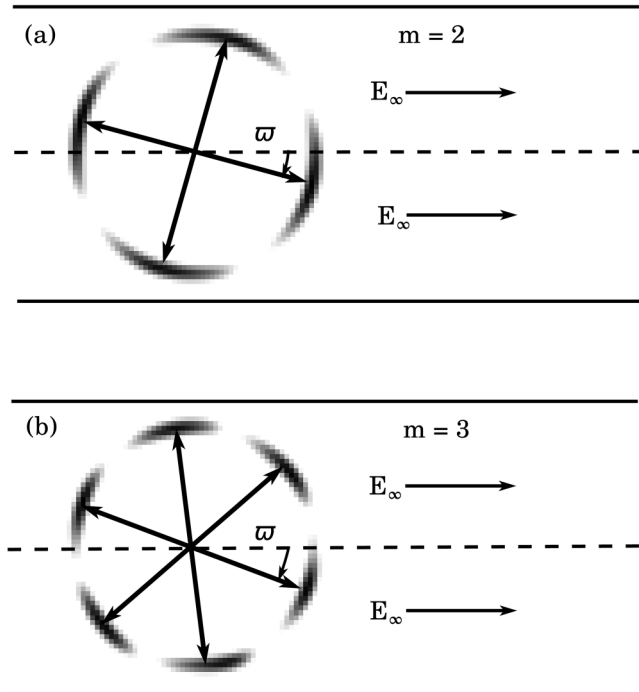


FIG. 1. Schematic of anisotropy in adatom mobility of island for (a) fourfold ($m = 2$) and (b) sixfold ($m = 3$). The double-headed arrows define positions of fast diffusion directions. Misorientation angle, ϖ , is defined with respect to the direction of the external electric field. E_∞ denotes the externally applied electric field from the cathode to the anode end.

III. RESULTS

We perform a detailed study and analysis of the numerical results obtained from phase-field simulations on the electromigration-induced dynamics of fourfold and sixfold islands. The order of various physical parameters provided in Table I has been ascertained from previously published experimental and numerical studies on island drift. The parameters $\chi (= q_s R_0^2 E_\infty / \Omega \gamma_s)$, Λ , A , and m provided in Table I are held fixed, while ϖ and $\beta = \sigma_{mat} / \sigma_{isl}$ are systematically varied to observe the morphological changes and migration modes of initially circular islands. The two extreme cases $\beta = 1$ and 10 000 correspond to single-layer homoepitaxial adatom islands and vacancy cluster, respectively. The intermediate cases correspond to precipitate-matrix systems in interconnect lines^{16,17,53} and conducting species trapped in the void.^{20,22}

A. Morphological map

The anisotropy in the adatom mobility is a result of the distinct diffusivity in different directions of a given plane. In FCC crystals, $\langle 110 \rangle$ -type directions have the highest surface diffusivity.⁵⁷ The $\langle 100 \rangle$ plane contains four crystallographic directions $[0\bar{1}1]$, $[01\bar{1}]$, $[011]$, and $[0\bar{1}\bar{1}]$ as shown in Fig. 2(a) along which diffusion is the fastest. Similarly, the $\langle 111 \rangle$ plane consists of six fast diffusion directions $[\bar{1}\bar{1}0]$, $[\bar{1}10]$, $[0\bar{1}\bar{1}]$, $[01\bar{1}]$, $[10\bar{1}]$, and $[101]$, as shown in Fig. 2(b).

TABLE I. Values of parameters employed for the simulation study.

Name of the parameter	Symbol	Value
Electric field to capillary force ratio	χ	15
Line width to island radius ratio	Λ	6
Anisotropy strength	A	10
Symmetry parameter	m	Fourfold: 2 Sixfold: 3
Misorientation angle	ϖ	Fourfold: 0° – 45° Sixfold: 0° – 30°
Conductivity ratio	β	1–10 000
Atomic volume	Ω	$2 \times 10^{-29} \text{ m}^3$ ^{35,4}
Surface diffusivity	D_s	$3.99 \times 10^{-10} \text{ m}^2/\text{s}$ ^{25,55}
Surface layer thickness	δ_s	$2.86 \times 10^{-10} \text{ m}$ ^{20,55}
Absolute temperature	T	419 K ^{55,56}
Boltzmann constant	k_B	$1.38 \times 10^{-23} \text{ J/K}$
Surface energy	γ_s	1.4 J/m^2 ²⁴
Effective charge	q_s	$20 \times 1.6 \times 10^{-19} \text{ C}$ ^{25,33}
Radius of initial island	R_0	525 nm ^{25,29}
Applied electric field	E_∞	476 V/m ^{25,29}

In fact, each planes in $\{100\}$ and $\{111\}$ families contain four and six of $\langle 110 \rangle$ directions and are referred to as fourfold and sixfold, respectively. Due to the symmetry of initial island shape, the parameter space of the misorientation ϖ can be reduced to a range from 0° to $45^\circ (= 180^\circ / 2m)$ for fourfold symmetry and from 0° to 30° for sixfold symmetry, without compromising the features of island morphology. In the systematic study of fourfold and sixfold symmetrical islands, the complex dynamics of island shape is obtained as a function of the misorientation angle ϖ and the conductivity ratio $\beta = \sigma_{mat} / \sigma_{icl}$, where σ_{mat} denotes the conductivity of the matrix and σ_{icl} represents the conductivity of the island.

Several island morphologies can be observed during propagation under electromigration-induced surface diffusion. Figures 3(a) and 3(b) present morphological maps of different migration modes in the β and ϖ plane obtained by the phase-field simulations for anisotropic fourfold and sixfold symmetries of adatom mobility, respectively. The islands exhibit various morphologies such as breakup, steady-state, time-periodic, and zigzag oscillations for sixfold symmetry, while only former three migration modes can be identified for the fourfold symmetrical islands. Kinetics of the different regions within a particular migration mode in the maps can be recognized by the distinct metrics such as perimeter and velocity during propagation. Each characteristic regions in the morphology maps are described in detail.

B. Steady-state morphology

The simplest morphology observed in both the symmetry cases is the steady-state. After an initial transition, the island assumes a specific shape depending upon the numerical parameters and maintains it while subsequent migration. For the selected values of χ , Λ , and A , the steady-state is observed at higher

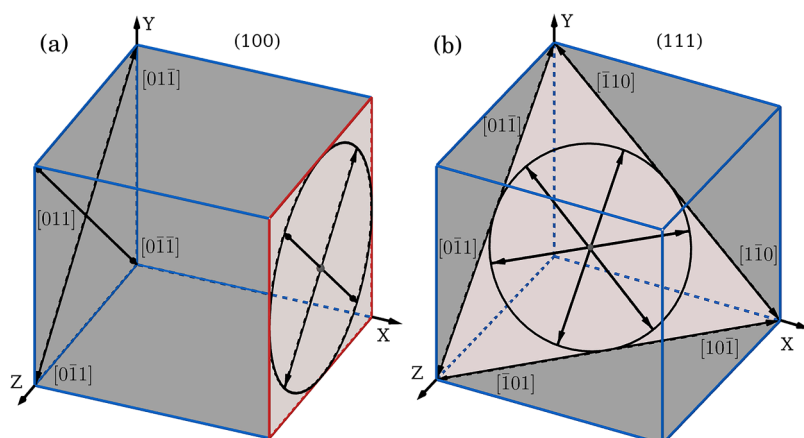


FIG. 2. Schematic of an island in the (100) crystallographic plane in (a) and the (111) plane in (b). The directions of dominant atomic diffusivity are represented by black arrows. The red color plane is the surface of the film perpendicular to the cylindrical islands.

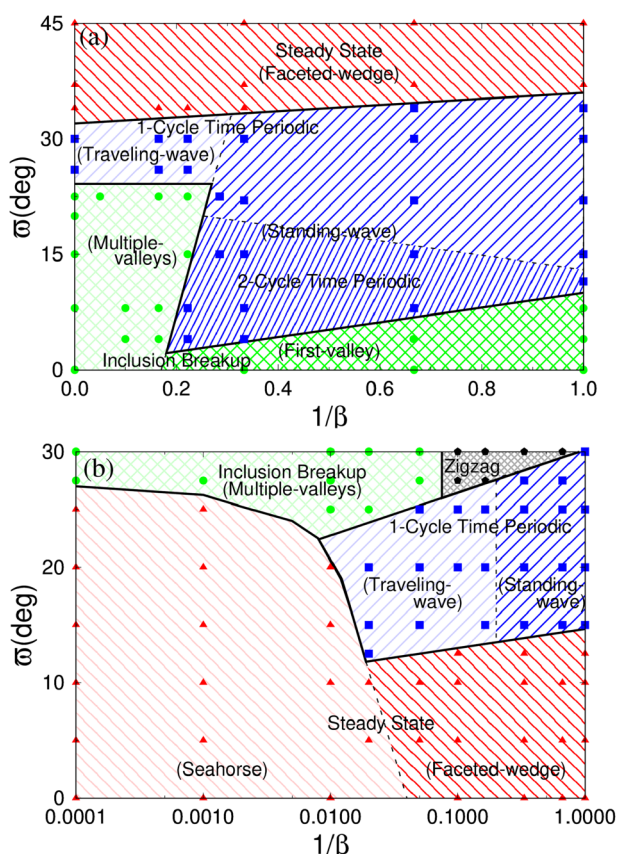


FIG. 3. Morphological maps of island migration modes as a function of β and ω for anisotropic fourfold ($m = 2$) symmetry in (a) and sixfold ($m = 3$) symmetry in (b). The triangular, square, pentagonal, and circular points in the map correspond to steady-state, time-periodic, Zigzag oscillations, and breakup states, respectively. The solid-black colored lines are a guide to the eye to differentiate between different modes of migration, while the dotted lines separate distinct characteristics of a particular migration mode. Semi-log plot is employed for the map of the sixfold symmetry for better visual representation.

misorientation in fourfold symmetry and lower misorientation in sixfold symmetry (red regions in Fig. 3).

A couple of representative temporal morphological evolutions for sixfold symmetry is shown in Figs. 4(a) and 4(b). Owing to the sixfold diffusional anisotropy, at $\omega = 10^\circ$ and $\beta = 1$ [Fig. 4(a)], the circular island initially assumes a hexagonal faceted shape at $t = 100\tau'$. The subsequent evolution ($t = 200 - 1800\tau'$) is governed by a facet selection mechanism,⁵⁸ where the bottom horizontal and the upper right tilted facets grow at the expense of the lower right tilted facet. The upper and lower facets at the rear end also shrink overtime but are not completely eliminated giving it an appearance of a faceted-wedge.

On the contrary, at higher $\beta (= 10000)$ and keeping ω unaltered in Fig. 4(b), the upper left and lower right tilted facets overgrow the bottom horizontal facet at initial stages ($t = 300\tau'$). At $t = 600\tau'$, the lower right tilted facet diverges into two new facets. The newly developed facets at the migrating front overgrow the lower right tilted parent facet at $t = 900\tau'$. The facet selection competition leads to the final shape resembling a seahorse.

The contrasting nature of the morphological evolution can also be seen by tracking the temporal evolution of the normalized island perimeter (instantaneous perimeter over initial perimeter). For the faceted-wedge morphology, the normalized island perimeter increases with time due to the elongation of the preferred facets as mentioned above and attains a constant value. The normalized perimeter of the seahorse structure, on the other hand, attains a maximum corresponding to the extension of the newly formed facet. Subsequently, the perimeter decreases due to the readjustment of the island shape to seahorse morphology.

After the islands attain an invariant shape, the steady-state velocities of the center of mass for fourfold and sixfold symmetries are obtained from phase-field simulations for different values of β as shown in Fig. 5 (blue and green curves, respectively). Also, for comparison, the velocity of a shape-preserving cylindrical island (pink curve) is derived from Ho's analytical formula.⁸ Along with that, velocities of islands migrating under isotropic diffusion ($m = 0$) and twofold symmetry ($m = 1$) obtained from phase-field simulations of Ref. 40 are also plotted. According to the classical result of Ho,⁸ the velocity of the cylindrical island migrating while

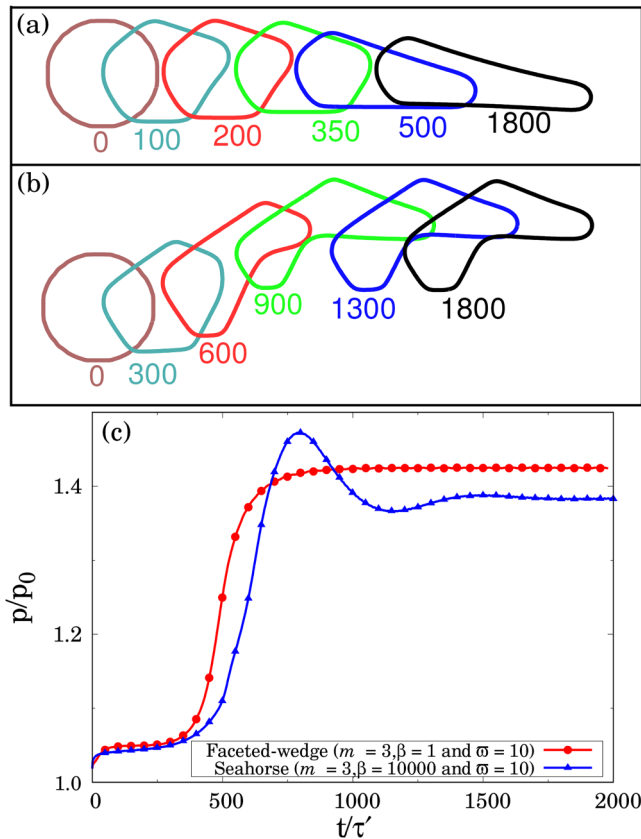


FIG. 4. Steady-state morphological evolution of faceted-wedge in (a) and seahorse pattern in (b). The island dynamics are shown for sixfold symmetry at misorientation angle $\varpi = 10^\circ$ and conductivity ratios $\beta = 1$ and 10 000, respectively. The islands with surface contours are presented with time, $t(\tau')$. The islands are displaced in space for better visual inspection. (c) represents the evolution of the normalized islands perimeter until it attains equilibrium shape.

preserving its shape decreases as the conductivity of the island increases with respect to the matrix (i.e., $1/\beta$ increases) as evident from the pink curve. However, depending on a critical value of χ for a given β , a cylindrical island undergoes a shape bifurcation to a slit. A slit propagates faster than a shape-preserving cylindrical island. Besides, the velocity of a narrower slit is higher compared to the thicker one as evident from the black curve. With the introduction of diffusional anisotropy, the velocity of the resulting structures decreases substantially than that of the isotropic case with the trend in general following the inequality sixfold > fourfold > twofold. Even though the symmetrical islands along the electric field are considered for the comparison in Fig. 5, a similar trend is also observed for other values of ϖ .

In terms of morphology, fourfold symmetry reveals a progressive increment in the width of the island and a decrement in the length with the increase in conductivity contrast β . A sudden shrinkage in the length (along with expansion in width) and

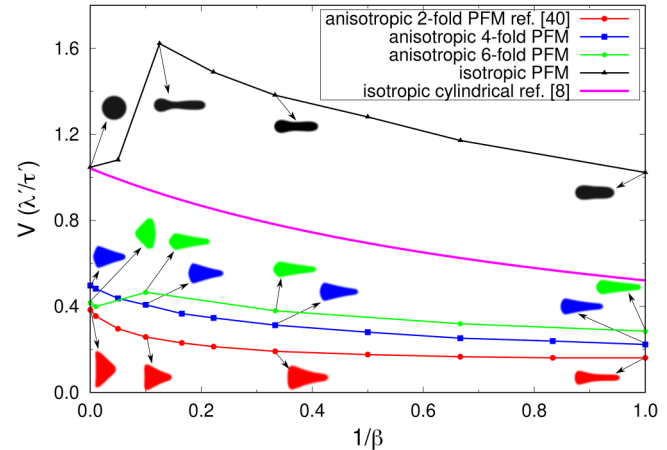


FIG. 5. The velocities of the center of mass of steady-state islands for twofold anisotropy ($m = 1$), $\varpi = 0^\circ$ (in circular points—red color) taken from Ref. 40, fourfold anisotropy ($m = 2$), $\varpi = 45^\circ$ (in square points—blue color), sixfold anisotropy ($m = 3$), $\varpi = 0^\circ$ (in pentagonal points—green color), and for isotropic ($m = 0$) surface diffusion (in triangular points—black color) as a function of the conductivity ratio β . The inset of images correspond to steady-state morphologies of, respective, m and β . The thick-pink-color curve corresponds to a steady-state velocity of the cylindrical island of isotropic surface diffusivity, derived from Ref. 8, considering the diffusion coefficient D_s . Evidently, β governs the island shapes and the steady-state velocities.

decrement in the velocity of the island from conductivity contrast $\beta = 10$ to $\beta = 10\,000$ are observed for sixfold symmetry, which is analogous to the isotropic case (black curve).

Even though nearly all islands attain a finger-like slit with thinner front and wider back for lower conductivity contrast ($\beta = 1$), different morphologies are observed for highest conductivity contrast ($\beta = 10\,000$). Twofold symmetry encourages triangular shape with the apex at the front, while sixfold symmetry promotes nearly a triangular shape with the apex at the back. From the velocity graph, it is evident from the green curve (for sixfold) that the flatter front with the apex at the back significantly restricts island velocity, while the apex at the front in the direction of motion with the flatter back (red inset at $\beta = 10\,000$ for twofold) assists the velocity of island migration.

C. Time-periodic oscillations

The intermediate misorientation of fast diffusion sites with the external electrical field promotes time-periodic oscillations for both the symmetries (blue regions in Fig. 3). Only low conductivity contrast ($\beta < 100$) shows time-periodic oscillations for sixfold symmetry, contrary to all the conductivity contrast for fourfold symmetry. The characteristic feature of the island undergoing time-periodic oscillation is an upper flat edge accompanied by a series of hills and valleys at the bottom edge as shown in Fig. 6. The island migrates in the direction of the upper flat edge. The morphologies can be further sub-categorized based on either the relative position of the valleys during motion or according to the amplitude of the normalized perimeter that is taken to be a metric of periodicity.

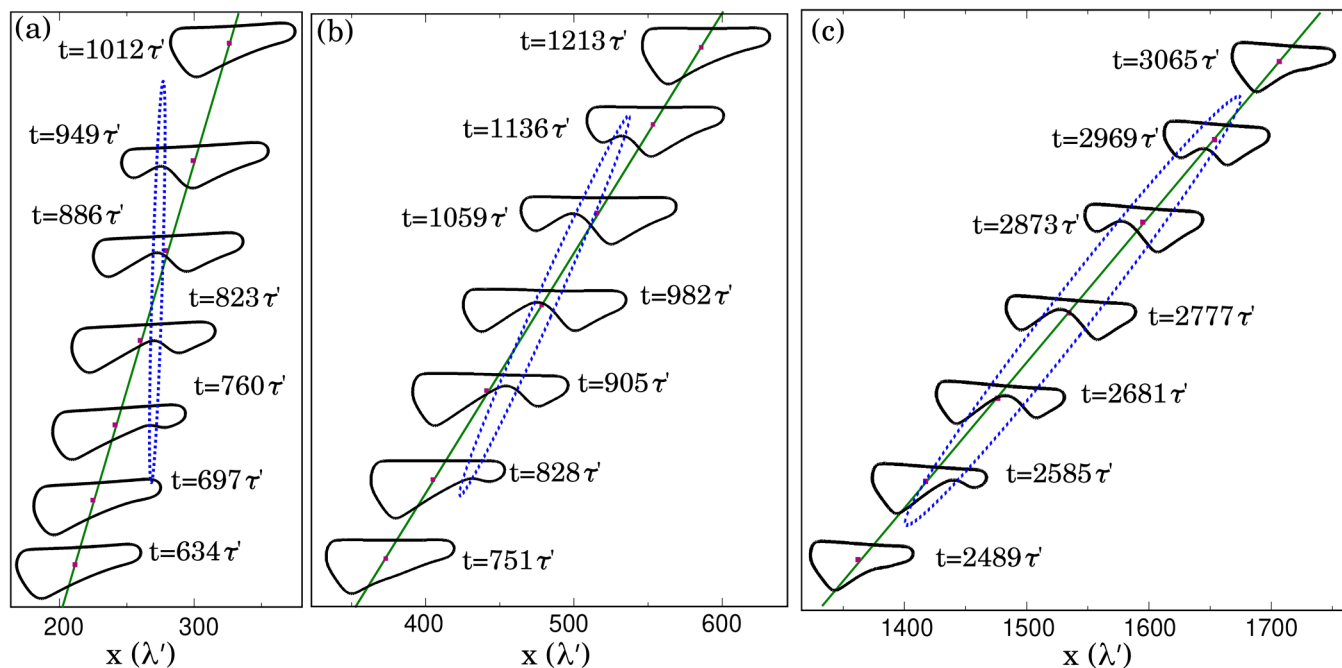


FIG. 6. The time-periodic shape dynamics of islands from standing-wave in (a) to traveling-wave in (b) and (c). The islands are shown for fourfold symmetry at misorientation angle, $\varpi = 30^\circ$ during the morphological evolution of an island with $\beta = 1$ in (a), 6 in (b), and 10 000 in (c). The snapshots of the islands are shifted upward in time. The solid green line passes from the center of mass. The dotted-blue ellipse is an attempt to recognize island gliding by incorporating the position of the valleys during evolution. The vertical ellipse indicates no gliding, while the slanted ellipse demonstrates degree of gliding. The island with equal conductivity to the matrix shows no appreciable gliding. The island of higher conductivity contrast shows relatively more gliding compared to the lower one.

1. Types of spatial wave during propagation

When the position of valleys and peaks within a period of oscillation is invariant in space, the morphology is termed as a standing wave. Contrarily, in the traveling wave case, the position of valleys and hills undergoes spatial displacement in the direction of island movement, which appears as a gliding of islands in the matrix.

An example of an island undergoing a standing wave oscillation for the fourfold symmetry at $\varpi = 30^\circ$ and $\beta = 1$ is presented in Fig. 6(a). At $t = 634\tau'$, the island adopts a slit-like shape with a protrusion at the rear end almost perpendicular to the direction of migration. With time ($t = 760\tau'$), a new protrusion develops at the forepart. The amplitude of the new protrusion increases with time and shifts toward the right. The amplitude of the protrusion at the rear end decreases simultaneously. At $t = 1012\tau'$, the island reverts to the original shape implying the completion of a period. It is evident that during the periodic cycle, the position of the single valley does not change in space as highlighted by the dotted-blue ellipse.

With an increase in conductivity contrast to $\beta = 6$ and 10 000 and keeping ϖ unchanged [Figs. 6(b) and 6(c)], although the shape of the island and the wave-like motion on the lower surface is similar to the previous case, the position of valley translates in space as evident from the dotted-blue ellipse. For the same ϖ , higher β promotes a traveling wave feature. In addition, even

though both islands (standing wave and traveling wave) attain their respective initial configurations after the completion of cycles as shown at $t = 1012\tau'$ in Fig. 6(a) and $t = 3065\tau'$ in Fig. 6(c), different evolutionary pathways are observed during the motion. By displacing islands to overlap center of mass as shown in Fig. 7, valleys are traced by a dashed-gray line. The valleys of standing wave are aligned in a straight line [Fig. 7(a)], while a curved path is observed for traveling wave morphology [Fig. 7(b)].

The island evolution for both types of time-periodic oscillations at the end of their respective cycles is shown in Fig. 8. Although the fresh protrusion at the leading edge increases with time at the expense of the rear one in both the cases, the rear protrusion is not completely eliminated at higher $\beta (= 10000)$. Rather, toward the end of the cycle when the two hills are of similar heights at $t = 2995\tau'$ in Fig. 8(b), the growth characteristic reverses and the one at the leading end decreases at the expense of the rear one as evident at $t = 3005 - 3065\tau'$.

The distinction between the standing and traveling time-periodic oscillations can be further supported by the plots of the center of mass velocity. The velocity plots of standing and traveling wave islands are demonstrated in Figs. 9(a) and 9(b), respectively. The dotted line represents the average velocity. The island velocities at the lower conductivity ratio peak in the region of the end of the cycle where the elimination of the older hill is about to complete, for instance, between $t = 1008$ and $1012\tau'$ in Fig. 8(a).

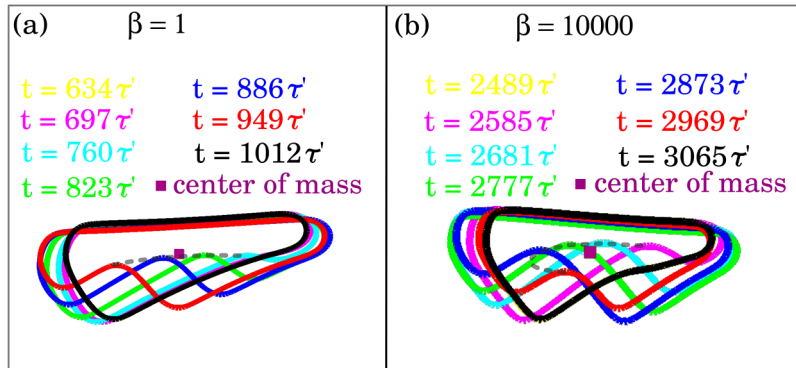


FIG. 7. Time-periodic morphology of islands for fourfold symmetry ($m = 2$) at misorientation angle, $\varpi = 30^\circ$ with $\beta = 1$ (standing wave) in (a), and 10 000 (traveling wave) in (b). The islands are displaced in space to overlap the center of mass. The dashed gray line traces valleys during evolution.

This behavior is demonstrated for $\beta = 1.0, 1.5,$ and 3.0 in Fig. 9(a). However, no appreciable deviation is observed around the average center of mass velocities in the case of traveling wave islands, as shown in Fig. 9(b) for $\beta = 4.5, 6.0,$ and $10\,000$. In addition, the mean center of mass velocity of the islands is continuously increasing with the increase in β irrespective of the type of motion.

Velocities of two extreme ends on the top (fixed) facet are considered along with the velocity of center of mass in Fig. 10. Tip velocity of the standing wave island appears to be constant, while base velocity increases drastically at the elimination of hill, which significantly affects the center of mass velocity. On the other hand, fluctuations in both (tip and base) velocities are comparable in traveling wave islands. Therefore, there is no significant deviation in the center of mass velocity during evolution.

Furthermore, the evolution of perimeters of standing and traveling wave islands is shown in Figs. 9(c) and 9(d), respectively. The increase in conductivity contrast increases the amplitude and the period of standing wave oscillation, while the increase in the

conductivity contrast increases the period and decreases the amplitude of the traveling wave oscillation. A similar trend is observed for various β of the sixfold symmetrical islands for both types of motion.

In Fig. 9(a), there are three sub-periods for each periodic response of velocity with respect to time. However, the corresponding evolution of the normalized perimeter plotted in (c) does not show any such behavior. A qualitatively similar result is observed in (b) and (d). To understand the connection between the wavefront at the periphery and evolution dynamics, a single period of representative time-periodic island is considered in Fig. 11. One period of island evolution can be divided into five distinct regions:

- Region-I ($t = 634 - 725\tau'$): During this part of evolution, only one hill is observed on the lower side of the island. As protrusion develops on the front part of the island, the perimeter steadily increases while no appreciable deviation observed in velocity.
- Region-II ($t = 725 - 760\tau'$): As a valley initiates on the lower side during this part of evolution, the perimeter evolution deviates from the previously observed linear trend. Similarly, velocity increases linearly compared to the previously observed constant value.
- Region-III ($t = 760 - 886\tau'$): After the initialization of valley, it traverses along the lower side. The perimeter increases continuously to attain a maximum value, while the velocity remains nearly unchanged. Note that at maximum value of perimeter, the valley is approximately in the middle of two equal sized hills.
- Region-IV ($t = 886 - 987\tau'$): Once the island attains a maximum perimeter, velocity of the island increases rapidly, while perimeter decreases. In this part, valley travels from center of the lower side to the end of the lower side.
- Region-V ($t = 987 - 1012\tau'$): Due to the elimination of the valley in the last part of the period, velocity of the island increases drastically. After the elimination of the valley, a sudden drop in velocity is observed to reach a single hill morphology.

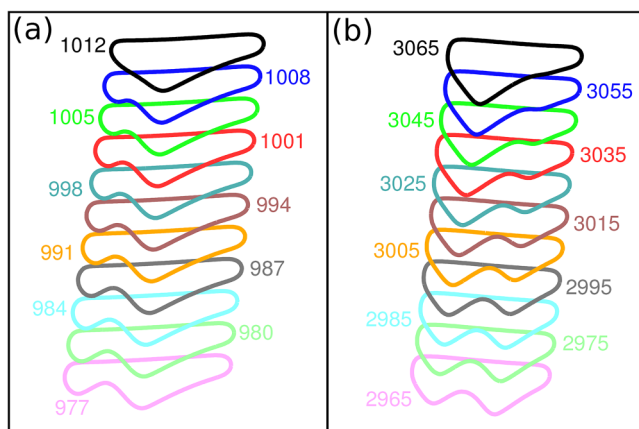


FIG. 8. (a) Standing-wave and (b) traveling-wave time-periodic shape dynamics of fourfold islands at misorientation angle $\varpi = 30^\circ$ during the morphological evolution at conductivity ratios $\beta = 1$ and $10\,000$, respectively. The islands with surface contours are presented with time, $t(\tau')$. The islands are displaced in space for better visual inspection.

Next, the effect of misorientation in fourfold and sixfold symmetrical islands on the different types of motion is highlighted in Fig. 12. A contrasting behavior is observed between fourfold and sixfold islands. For instance, the amplitude of standing wave motion of fourfold island depreciates and the period enhances with ϖ , which is contrary to sixfold islands. Similarly, a reversed trend is

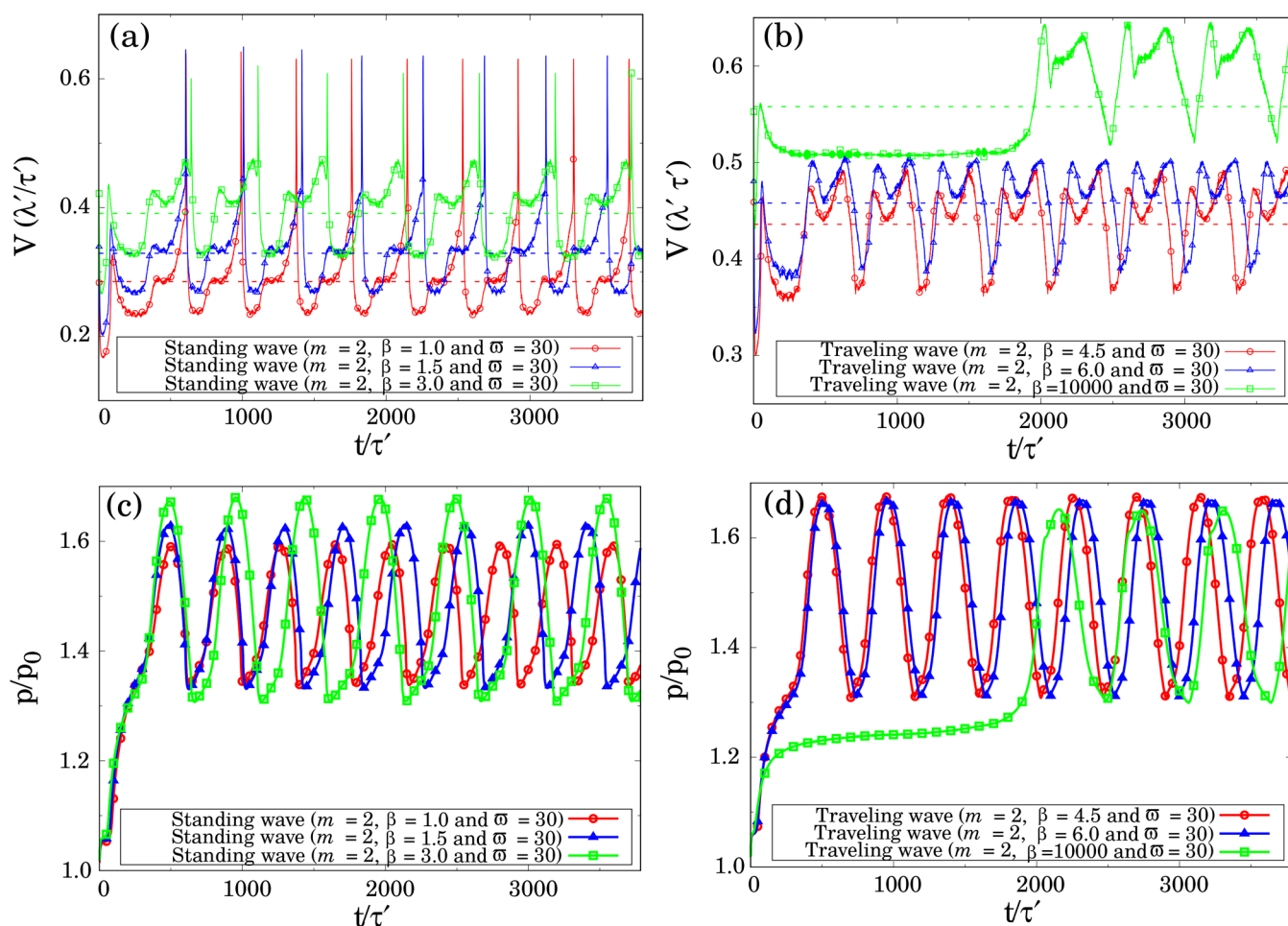


FIG. 9. Effect of conductivity contrast during the morphological evolution of standing-wave and traveling-wave time-periodic oscillations. The islands are shown for misorientation angle $\varpi = 30^\circ$ and various values of conductivity contrast β . The center of mass velocity of islands is demonstrated for standing waves in (a) and traveling waves in (b), while the normalized perimeter is shown for standing waves in (c) and traveling waves in (d). The dotted lines in the upper panel of the graph are mean center of mass velocity of a complete period of respective solid curves.

observed between the fourfold and sixfold islands during traveling wave kinetics. This behavior can be rationalized from the location of the time-periodic region in the phase diagram. Meaning, steady-state morphology is situated above the time-periodic region in the fourfold, while below in the sixfold symmetry. The steady-state morphology can be perceived as time-periodic oscillation with an infinite period. Therefore, the islands at highest ϖ in fourfold [blue curves in Figs. 12(a) and 12(b)] and lowest ϖ in sixfold symmetry [red curves in Figs. 12(c) and 12(d)] show oscillations of highest periods compared to their counterparts.

2. Types of periodic cycles

Depending on the amplitude of the normalized perimeter, the periodic oscillation can be differentiated as 1-cycle or 2-cycle time-periodic motion.

A representative simulation of a 1-cycle and 2-cycle period for a four-fold symmetry is presented in Figs. 13(a) and 13(b), respectively. 1-cycle morphology is characterized by a stable flat facet at the top edge and a standing wave with a single valley at the bottom edge. In a given period, the valley commutes from the front to the rear end of the island. In a 2-cycle period, the bottom edge of the island is characterized by the two valleys [Fig. 13(b) $t = 354\tau'$]. A period of oscillation is attained when the valley traverses a distance equal to the difference between the initial positions of the two neighbor valleys. The second valley present at $t = 354\tau'$ shifts toward the rear end and eventually disappears at $t = 420\tau'$. During the intermediate stages ($t = 420 - 519\tau'$), the bottom edge consists of only a single valley.

The difference between the 1-cycle and 2-cycle state is evident from the plot of the normalized perimeter in Fig. 13(c). While the

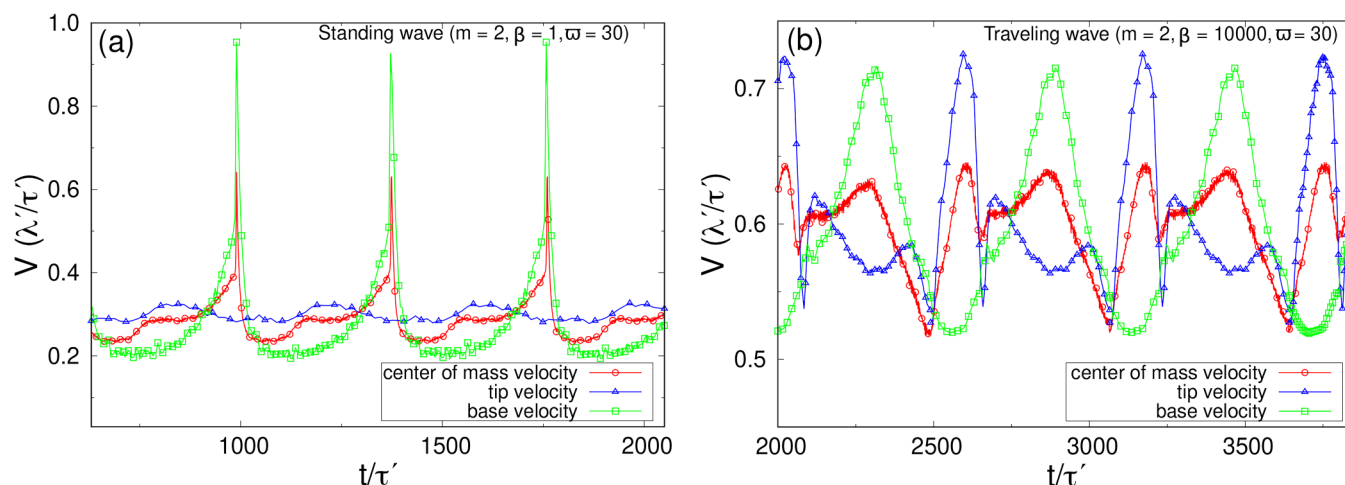


FIG. 10. Velocities of center of mass, tip, and base for standing wave ($m = 2, \beta = 1$, and $\varpi = 30^\circ$) in (a) and traveling wave ($m = 2, \beta = 10000$, and $\varpi = 30^\circ$) in (b).

1-cycle periodic state is characterized by a single amplitude, the 2-cycle periodic state exhibits a dual amplitude. The appearance and disappearance of valleys during the course of morphological evolution are presented in Fig. 13(d). In a 1-cycle periodic motion, the island oscillates between a state of the null and single valley. Besides, a 2-cycle periodic state oscillates between a single and double valley.

The effect of β on the dynamics of 1-cycle and 2-cycle is displayed in Figs. 14(a) and 14(b), respectively. Increasing β enhances the amplitude of the perimeter along with the increment in the

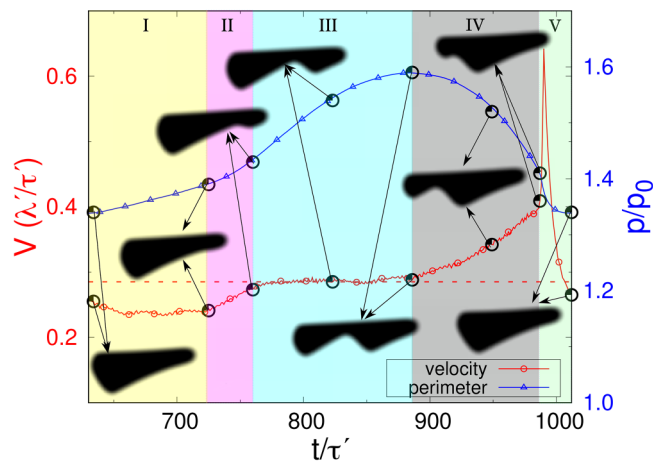


FIG. 11. Superimposed velocity and perimeter of island evolution for a one period of representative time-periodic oscillations ($\beta = 1, \varpi = 30^\circ$, and $m = 2$). Inset of images is the island morphology at respective time. Region of evolution is sub-divided into five parts based on their typical features. The red dashed-line represents the average migration velocity of the island over a time-period.

period for 1-cycle oscillations, which is contrary to 2-cycle. Furthermore, the mean perimeter exhibits a significant disparity. The mean perimeter is approximately equal for all cases of the 1-cycle state, while the value of mean perimeter increases with β for the 2-cycles state.

D. Island breakup

The island breakup can be observed for all values of conductivity contrast at low misorientation in fourfold symmetry, as compared to only high misorientation along with high conductivity contrast for sixfold symmetry. An island breaks up either after the formation of (i) a single valley or (ii) the multiple valleys on the lower edge of the island. Both cases can be observed for fourfold symmetry, while only the latter is evident for sixfold symmetry.

A representative case for a fourfold symmetry at $\varpi = 0^\circ$ is described in Fig. 15. At lower conductivity ratio ($\beta = 1$), the island forms a slit-like feature with a narrow front and a protruded end as shown in Fig. 15(a) at $t = 1611\tau'$. Subsequently, similar to time-periodic state, a valley develops at the front end ($t = 1621\tau'$) and migrates toward the end ($t = 1631\tau' - 1701\tau'$). However, during the displacement, the depth of the valley increases over time leading to a pinch-off at the center of the island. At higher conductivity ratio $\beta = 10000$, however, multiple valleys form at the lower edge before the pinch-off event takes place when the first valley reaches the rear end of the island.

The normalized perimeter in Fig. 15(c) increases with time until the break up as fresh surfaces are exposed due to the increase in the depth of the valley. The formation of multiple valleys increases the normalized perimeter in a step-like fashion beyond that of the previous case, before the island eventually breaks up.

E. Zigzag oscillations

For the selected parameter space, the zig-zag oscillations are observed only for sixfold symmetry with higher misorientation and

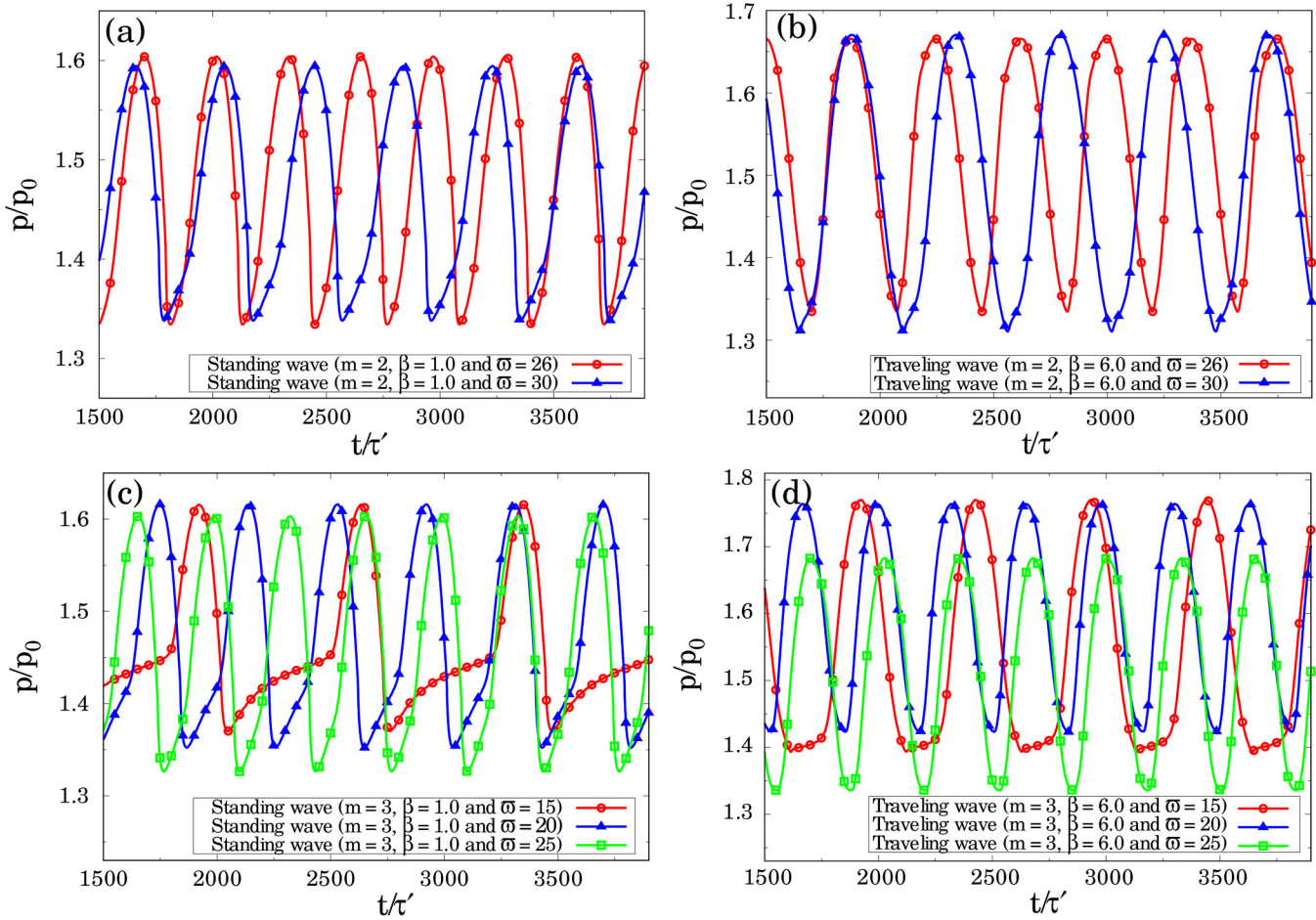


FIG. 12. Evolution of the perimeter as a function of ω . The normalized perimeter of fourfold symmetrical islands is displayed for standing waves in (a) and traveling waves in (b), while the normalized perimeter of sixfold symmetrical islands is shown for standing waves in (c) and for traveling waves in (d).

lower conductivity ratio ($1/\beta \approx 0.1-1.0$). A representative morphological evolution is displayed in Fig. 16 for $m = 3$, $\beta = 6$, and $\varpi = 28^\circ$. Contrary to the time-periodic oscillations, where a straight edge on one side remains permanently impervious, while the hills and the valleys on the other side undergo shape changes during propagation (for instance in Fig. 6); the zigzag oscillations are a result of the reversal of the straight edge from the upper to the lower facet during evolution. Similar to the time-periodic oscillation, a valley traverses from the lower front to the rear end ($t = 800 - 1000\tau'$) but then moves to the top edge ($t = 1200\tau'$). The normalized perimeter shown in Fig. 16(b) exhibits complex oscillatory dynamics with an unclear pattern.

As evident in Fig. 16, certain facets are preferably stable during the course of evolution. The stability of a facet with slope m can be evaluated from the continuum theory^{32,59,60} by estimating the growth or the decay of an imposed perturbation.

For arbitrary shape and conductivity ratio, an implicit form of the shape function $g(\theta, \beta)$ is non-trivial to compute analytically,

and the stability of a facet needs to be assessed via numerical simulations. However, an analytical relation can be derived by considering a simplified equation, $g(\theta, \beta) = g_1(\beta) \cos \theta$, where $g_1(\beta)$ is a function of the conductivity ratio. In this case, the electric field is approximated by surface projection, and the stability criterion reduces to

$$f(\theta) \tan \theta - \frac{df(\theta)}{d\theta} < 0. \tag{3}$$

The full derivation is provided in Appendix. The resulting stable facet orientations $\theta^* = \theta$ are derived for the required anisotropy parameters. These orientations are displayed as dotted lines in Figs. 16(a1) and 16(a2). Interestingly, the stable facets observed in numerical simulations agree well with the above condition. Therefore, the assumed form of the shape function appears to be an excellent approximation. In fact, this kind of expression (i.e., $g(\theta, \beta) = g_1(\beta) \cos \theta$) for electric field projection on the island

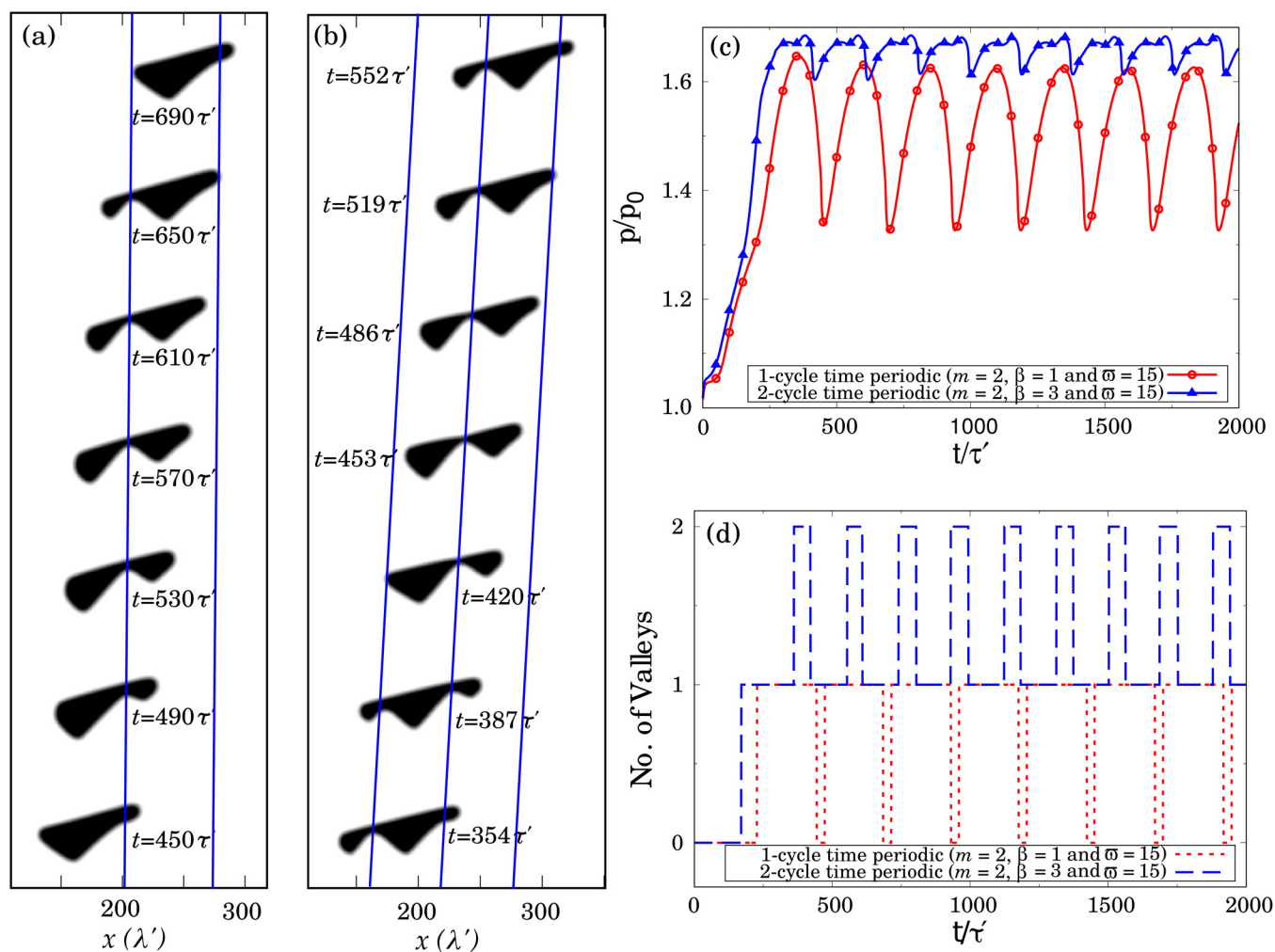


FIG. 13. cycle time-periodic in (a) and 2-cycle time-periodic in (b). The island morphologies are shown for fourfold island at misorientation angle $\varpi = 15^\circ$ at conductivity ratios $\beta = 1$ and 3 respectively. The snapshots of the islands are shifted upward in time. (c) represents the evolution of the normalized islands' perimeter and (d) shows the number of valleys (locations of negative curvature) during island propagation.

surface is considered widely in previous analytical^{16,33,34} and numerical^{20,22,34,40} studies.

IV. DISCUSSION

The dependence of stability on the misorientation for the sixfold symmetry is qualitatively similar to the twofold symmetry.⁴⁰ In terms of morphology, increasing the symmetry fold enhances the richness of the migration modes and morphological characteristics. Higher symmetry fold promotes faceting, and hence, the seahorse structure with multiple facets is only observed in the sixfold case. In contrast, only slit-like and triangular islands were observed in the steady-state migration mode for lower (two-fold) symmetry.⁴⁰ While time-periodic oscillatory states are observed across all

symmetry folds, the resulting nano-structures were found to be different. Higher (four- and sixfold) symmetry assists an island with a straight top edge and a bottom edge with the wave-like feature. However, islands with straight bottom edge and wave on the top edge were observed in the twofold symmetry.⁴⁰ Similarly, break-up characteristics can also be studied to identify the symmetry modes. For instance, in the four- and sixfold symmetries, the island disintegrates at one of the valleys at the lower edge. On the other hand, for a twofold symmetry, the island pinches-off via necking instability on both lower and upper edges. A complex island multiplication was observed in the twofold case, which is found to be absent in four- and sixfold symmetries in the parameter space of interest.

The pre-existing island in the present work has been assumed to be circular in all the simulations. This assumption, however,

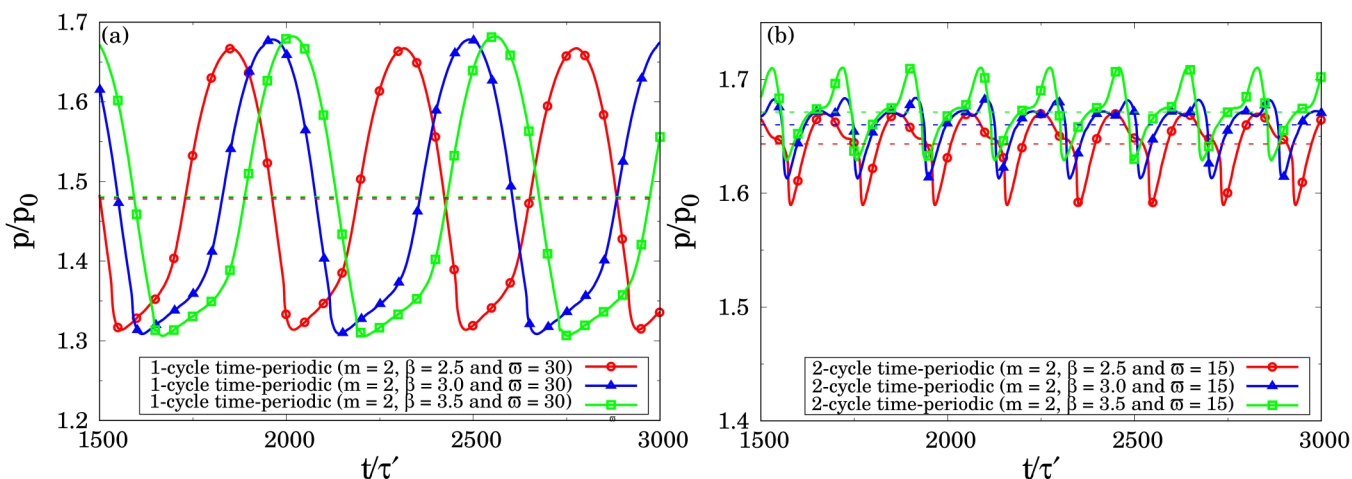


FIG. 14. Evolution of perimeter for (a) 1-cycle and (b) 2-cycle time-periodic oscillations as a function of β . The island morphologies are shown for fourfold island at misorientation angle $\varpi = 30^\circ$ and 15° , respectively. The dotted lines in the graph are the mean perimeter of a complete period of the respective solid curves.

needs not always to be true. An island, for example, may attain a shape depending on prior processing history. If any of the processing parameters such as the electric field, misfit stress, and temperature is altered, the subsequent evolution of the shape will depend on the prior processing history.^{61,62} Similarly, electrical conductivity is a material that may vary with processing conditions such as temperature.^{63,64} Therefore, understanding the effect of altering the conductivity during island migration has scientific importance.

To depict the significance of change in conductivity during island migration, we perform simulations, as shown in Fig. 17(a),

for $\beta = 1$ (red curve) and 10 000 (blue curve) for $m = 3$ and $\varpi = 10^\circ$. In addition, β is changed from 10 000 to 1 in the middle of simulation run at time $t = 1000\tau'$ (green curve). Due to the sudden change in the conductivity ratio, the island undergoes a shape adjustment but quickly transforms into a faceted-wedge from the initial seahorse structure. The trajectory of the perimeter exactly overlaps with the one in which $\beta = 1$ was maintained throughout the course of evolution. A similar observation was reported in Ref. 34 when the electric field was changed during evolution. However, this is true only for a few cases. For instance, segregated

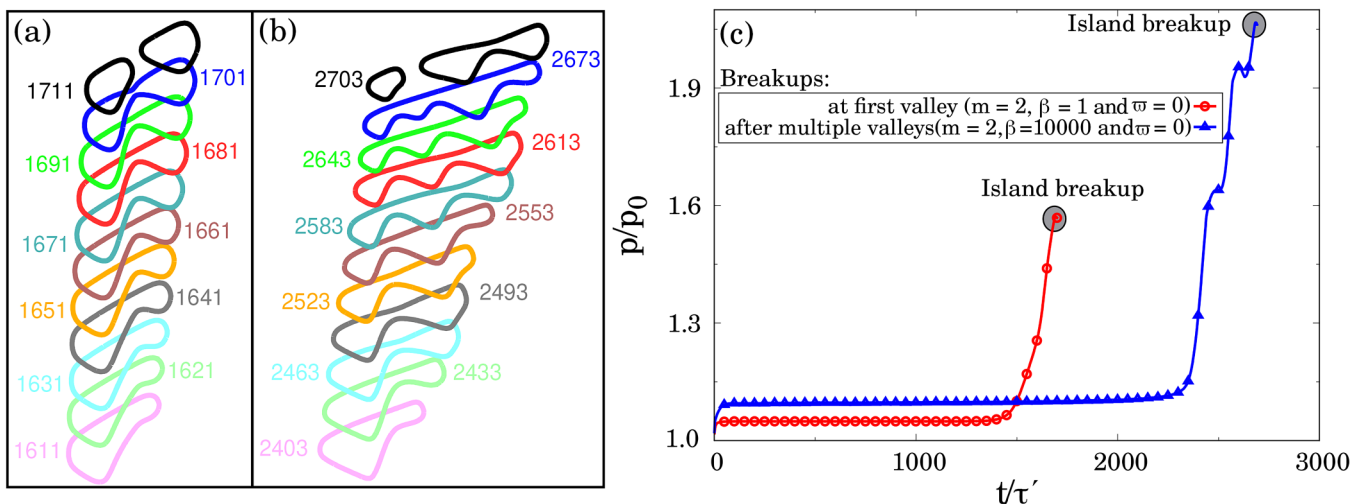


FIG. 15. Representative dynamics of island breakup at the first valley in (a) and after multiple valleys in (b). The island breakups are shown for fourfold island at misorientation angle $\varpi = 0^\circ$ during the morphological evolution at conductivity ratio $\beta = 1$ and 10 000, respectively. The islands with surface contours are presented with time, $t(\tau')$. The islands are displaced in space for better visual inspection. (c) represents the evolution of the islands' perimeter (normalized by initial island perimeter) until breakup.

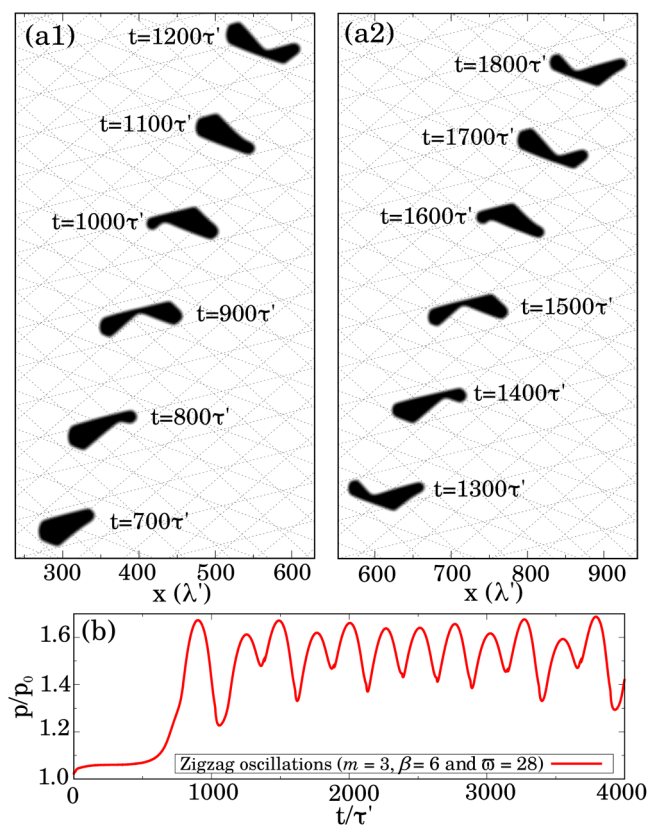


FIG. 16. (a) Zigzag oscillations of the sixfold symmetrical island at misorientation angle $\varpi = 28^\circ$ and conductivity ratio $\beta = 6$. The snapshots of the islands are shifted upward in time. The gray dotted lines represent preferential facet orientations predicted by the linear stability theory. (b) represents the evolution of the normalized islands' perimeter.

islands may not reassemble further, as shown in Fig. 17(b). After the breakup at $t = 620\tau'$, the parts of fourfold island with $\varpi = 15^\circ$ and $\beta = 10000$ further drifts apart (see blue insets on right-hand side). Even though the change in conductivity from $\beta = 10000$ to 1 (green curve) instigates time-periodic oscillations similar to the fully developed island $\beta = 1$ (red curve), the broken parts did not reassemble. Hence, the discrimination between two islands (fully developed as $\beta = 1$ and intermediate change from $\beta = 10000$ to 1) is clearly visible in perimeter evolution. Therefore, these observations necessitate further scrutiny, which should be performed in our future work.

Our results on the steady-state migration are an important generalization to the analytical theory of Ho,⁸ which was valid for island motion under isotropic diffusion. Although a non-linear decrease in velocity with $1/\beta$ remains valid for anisotropic diffusion, the decrease is much steeper in comparison to the isotropic case (Fig. 5). Faceted islands engendered due to anisotropic diffusion have lower velocity in comparison to the cylindrical islands migrating under isotropic diffusion. Furthermore, for anisotropic diffusion, the velocity increases with symmetry fold. In terms of morphology, increasing β increases the width of the island in the

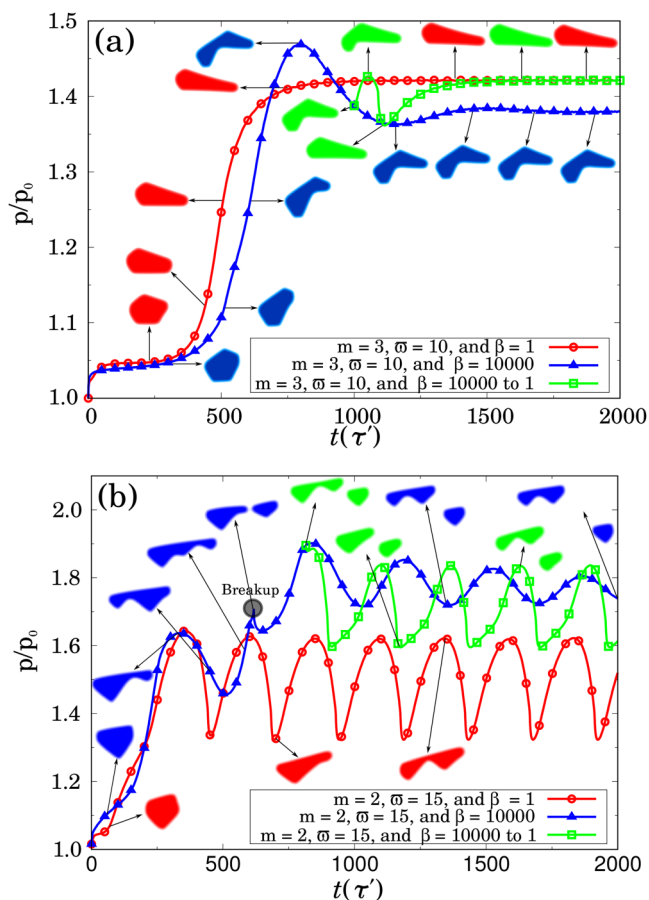


FIG. 17. The complex shape dynamics of (a) sixfold island at misorientation angle $\varpi = 10^\circ$ and (b) fourfold island at $\varpi = 15^\circ$ during morphological transformation. The evolution pathways of normalized perimeter are demonstrated as a function of time for conductivity ratio, $\beta = 1, 10000$, and the alteration of the conductivity ratio from $\beta = 10000$ to 1 after $t = 1000\tau'$ in (a) and $800\tau'$ in (b). The insets show island morphology during propagation.

direction perpendicular to the applied electric field. Such transverse elongation of vacancies can have a deleterious implication on the lifetime of metallic lines.

While we have used a broader term island, our results are applicable to vacancies, precipitates, and adatom clusters alike. For instance, the case of $\beta = 1$ corresponds to homoepitaxial islands on crystalline substrates. $\beta = 10000$ captures the dynamics of vacancy clusters in interconnect lines. The intermediate values of β correspond to precipitates in interconnects. For instance, Al_2Cu precipitates (resistivity $\rho_{\text{Al}_2\text{Cu}} = 6.5\mu\Omega\text{cm}^{53}$) are developed in bamboo lines to extend the lifetime of aluminum (resistivity $\rho_{\text{Al}} = 2.78\mu\Omega\text{cm}^{53}$) interconnects.¹⁷ The intermediate β also corresponds to the case where conductive species might be trapped inside the vacancy.^{20,22} It was shown by Hao and Li²² through a linear stability analysis that for an isotropic adatom mobility, the stability of the island is sensitive to the conductivity of the island

relative to the medium ($1/\beta$ in the present case). An insulating island ($1/\beta = 0$) is linearly stable even at higher values of the electric field ($\chi_{cr} \approx 400$, where χ_{cr} represents the critical value of χ above which the island is unstable), while a 10% conductivity of the island ($1/\beta = 0.1$) decreases χ_{cr} by approximately 20 times. Although the present study corresponds to anisotropic adatom mobility, it can be seen in Fig. 3 that the increase in $1/\beta$ decreases the steady-state region in the morphological diagram. A similar behavior was also observed for the twofold symmetry mode in Ref. 40. The effect of misfit strain has to be additionally accounted in such cases to faithfully capture the island dynamics similar to the front tracking simulations of Dasgupta *et al.*²⁷ However, as an initial step to understand island dynamics, the misfit strains are neglected and we emphasize the effect of conductivity contrast on island morphology.

A morphological diagram such as the one presented in Fig. 3 could serve as a guideline to control process parameters to fabricate nanostructures and enhance the lifetime of interconnect lines. In this regard, our results are complementary to several works of Maroudas and co-workers^{28,29,37} on island migration and generalize the results for the case of arbitrary conductivity ratios. Some of the morphologies presented here have been observed earlier albeit in different parametric space such as steady-state faceted-wedge islands,²⁹ time-periodic 1-cycle and 2-cycle standing wave states,²⁹ zigzag-type motion,²⁶ and island breakup due to pinch-off at the first valley.²¹ Other morphologies such as the periodic traveling wave state, breakup subsequent to the formation of multiple hills and valleys and seahorse structure are being reported for the first time.

V. CONCLUSION

A phase-field numerical study is presented to investigate islands migrating along the {100} and {111} planes of an FCC crystal. In particular, an emphasis is laid on understanding the effect of conductivity contrast (β) between the island and the matrix. The role of misorientation between the fast diffusion directions and the electric field has also been elucidated.

For a fourfold symmetry, i.e., an island migrating along the {100} plane, increasing misorientation angle stabilizes the shape of the island [Fig. 3(a)]. Islands undergo a morphological transition exhibiting break up, time-periodic state, and steady state with increasing misorientation. For a time-periodic state, increasing β leads to transformation from a standing wave to a traveling wave propagation on the surface of the island. The island breaks up via pinch-off at the first valley for lower β , while multiple valleys survive before a pinch-off occurs at the rear end for higher β .

For a sixfold symmetry, i.e., an island migrating along the {111} plane, the island shape is stabilized at a lower misorientation [Fig. 3(b)]. The island either breaks up at higher β or undergoes a zig-zag motion at lower β . Time-periodic motion is observed at intermediate misorientation and at lower β .

The island morphologies and dynamics can be tailored in order to form various interesting nanopatterns by monitoring the conductivity contrast. Even though a fixed value of the electric field is employed in the present work, numerous morphologies can be observed. The variety of morphologies can be further enhanced by

regulating the strength of the electric field or the size of the island. In addition, the incorporation of other fields, such as elasticity, flourishes the richness of patterns. The incorporation of elasticity has a physical significance and will be addressed in our upcoming works.

ACKNOWLEDGMENTS

The authors are grateful for financial support from the Helmholtz association through the programme “EMR = Energy, Materials, and Resources.” This work contributes to the research performed at CELEST (Center for Electrochemical Energy Storage Ulm-Karlsruhe) and was partially funded by the German Research Foundation (DFG) under Project ID 390874152 (POLiS Cluster of Excellence).

APPENDIX: STABILITY OF FACETS

The governing equation of island propagation is a result of capillarity and electromigration force given by the Nernst–Einstein relation,

$$J_s = \frac{D_s f(\theta) \delta_s}{\Omega k_B T} \left(-q_s E_t + \Omega \gamma_s \frac{d\kappa_s}{ds} \right), \quad (\text{A1})$$

where J_s is the atomic flux per arc length along the surface of island, E_t represents the tangential component of the electric field E_∞ along the island surface, $\theta = \tan^{-1}(dy/dx)$, $\kappa_s = (dy^2/dx^2)/[1 + (dy/dx)^2]^{3/2}$ denotes the local curvature of the surface, and s is the arc length along the island surface. The tangential electric field along the surface (E_t) is the function of shape (θ) and conductivity ratio (β), expressed as

$$E_t = E_\infty g(\theta, \beta), \quad (\text{A2})$$

where $g(\theta, \beta)$ is a shape function that gives the electric field distribution on the surface of the island.

Mass conservation relates the divergence of the surface flux to the normal velocity as

$$V_n = -\Omega \frac{dJ_s}{ds}, \quad (\text{A3})$$

where V_n denotes the normal velocity. By utilizing the relations, $dy/dt = V_n \cos \theta$ and $dx = ds \cos \theta$, the above equation can be expressed as

$$\frac{dy}{dt} = -\Omega \frac{dJ_s}{dx}. \quad (\text{A4})$$

The stability analysis of a facet $y = mx$ oriented at an angle θ in the anti-clockwise direction to the electric field, as shown in Fig. 18, is performed by introducing a perturbation of the form

$$h(x, t) = y(x, t) - mx. \quad (\text{A5})$$

Substituting Eqs. (A1), (A2), and (A5) in Eq. (A4) and simplifying,

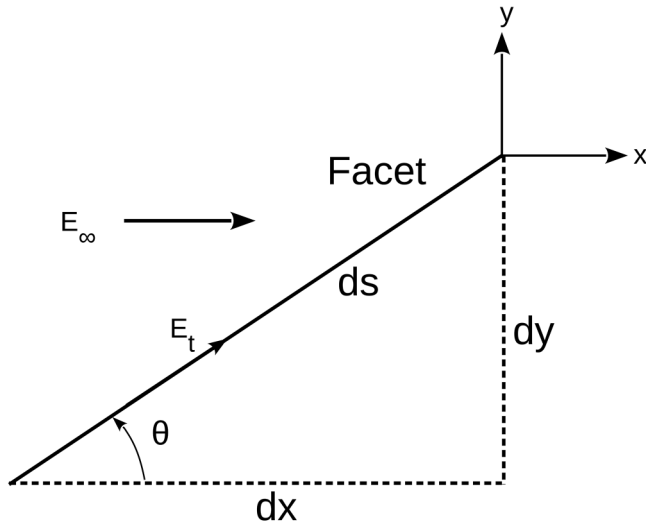


FIG. 18. Schematic of a facet of an island. Thick black line indicates the facet, which is subjected to an external electric field E_∞ . The projection of the electric field on the surface of facet is E_t .

the resultant equation can be represented as

$$\frac{dh}{dt} = \frac{D_s \delta_s q_s E_\infty}{k_B T} \left[\frac{d}{d\theta} \{f(\theta)g(\theta, \beta)\} \frac{1}{1+m^2} \frac{d^2 h}{dx^2} - \frac{\gamma_s \Omega}{q_s E_\infty} f(\theta) \frac{1}{(1+m^2)^2} \frac{d^4 h}{dx^4} \right], \quad (\text{A6})$$

where $m = \tan \theta = dy/dx$. The above equation can be simplified by considering the dimensionless variables of the form

$$\hat{h} = \frac{h}{a}, \quad \hat{x} = \frac{x}{a}, \quad \hat{t} = \frac{D_s \delta_s q_s E_\infty}{k_B T a^2} t, \quad \chi = \frac{q_s E_\infty a^2}{\gamma_s \Omega}. \quad (\text{A7})$$

Substituting these relations in Eq. (A6), the simplified equation is expressed as

$$\frac{d\hat{h}}{d\hat{t}} = \frac{d}{d\theta} \{f(\theta)g(\theta, \beta)\} \frac{1}{1+m^2} \frac{d^2 \hat{h}}{d\hat{x}^2} - \frac{1}{\chi} f(\theta) \frac{1}{(1+m^2)^2} \frac{d^4 \hat{h}}{d\hat{x}^4}. \quad (\text{A8})$$

Based on Eq. (A8), the dispersion relation is derived to encompass dimensionless frequency ω , which signifies the growth or the decay rate of perturbation as a function of the dimensionless wavenumber k of the form

$$\omega(k) = -\frac{d}{d\theta} [f(\theta)g(\theta, \beta)] \frac{k^2}{(1+m^2)} - \frac{f(\theta)}{\chi} \frac{k^4}{(1+m^2)^2}. \quad (\text{A9})$$

For the stability of the facet, the perturbation frequency $\omega(k)$ should be negative. As the second term in Eq. (A9) is always

negative, the facet is stable when

$$\frac{d}{d\theta} \{f(\theta)g(\theta, \beta)\} > 0. \quad (\text{A10})$$

For arbitrary shape and conductivity ratio, a closed form of the shape function $g(\theta, \beta)$ is non-trivial to compute analytically, and the stability of a facet can be assessed via numerical simulations. However, analytical forms can be obtained for following simplified cases:

- (1) For isotropic ($f(\theta) = 1$) and homogeneous ($\beta = 1$) case, $g(\theta, \beta) = \cos \theta$. Substituting these relations in Eq. (A10), the stability criterion for isotropic and homogeneous system^{60,65} can be simplified as $\tan \theta < 0$. This relation is also valid for the isotropic and heterogeneous ($\beta \neq 1$) case, when the shape function takes the form $g(\theta, \beta) = g_1(\beta) \cos \theta$. Note that this form is analogous to the shape functions utilized for circular islands,^{20,22,40} $g(\theta, \beta) = 2\beta/(1 + \beta) \cos \theta$.
- (2) For anisotropic ($f(\theta) \neq 1$) and homogeneous ($\beta = 1$) case, $g(\theta, \beta) = \cos \theta$. Substituting these relations in Eq. (A10), the stability criterion for isotropic and homogeneous system³² can be simplified as

$$f(\theta) \tan \theta - \frac{df(\theta)}{d\theta} < 0. \quad (\text{A11})$$

- (3) For anisotropic ($f(\theta) \neq 1$) and heterogeneous ($\beta \neq 1$) case, the shape function $g(\theta, \beta)$ needs to be computed numerically. However, for the explicit form of the shape function, $g(\theta, \beta) = g_1(\beta) \cos \theta$, Eq. (A11) shall also be applicable for stability.

DATA AVAILABILITY

The data that support the findings of this study are available from the corresponding author upon reasonable request.

REFERENCES

- ¹L. Xia, A. F. Bower, Z. Suo, and C. Shih, "A finite element analysis of the motion and evolution of voids due to strain and electromigration induced surface diffusion," *J. Mech. Phys. Solids* **45**(9), 1473–1493 (1997).
- ²R. Barnes and D. Mazey, "The migration and coalescence of inert gas bubbles in metals," *Proc. R. Soc. London Ser. A* **275**(1360), 47–57 (1963).
- ³A. Kunwar, B. Guo, S. Shang, P. Råback, Y. Wang, J. Chen, H. Ma, X. Song, and N. Zhao, "Roles of interfacial heat transfer and relative solder height on segregated growth behavior of intermetallic compounds in Sn/Cu joints during furnace cooling," *Intermetallics* **93**, 186–196 (2018).
- ⁴M. Mur, J. A. Sofi, I. Kvasić, A. Mertelj, D. Lisjak, V. Niranjan, I. Mušević, and S. Dhara, "Magnetic-field tuning of whispering gallery mode lasing from ferro-magnetic nematic liquid crystal microdroplets," *Opt. Express* **25**(2), 1073–1083 (2017).
- ⁵Z. Li and N. Chen, "Electromigration-driven motion of an elliptical inclusion," *Appl. Phys. Lett.* **93**(5), 051908 (2008).
- ⁶A. Kunwar, Y. A. Coutinho, J. Hektor, H. Ma, and N. Moelans, "Integration of machine learning with phase field method to model the electromigration induced Cu6Sn5 imc growth at anode side Cu/Sn interface," *J. Mater. Sci. Technol.* **59**, 203–219 (2020).

- ⁷A. Yamanaka, K. Yagi, and H. Yasunaga, "Surface electromigration of metal atoms on Si(111) surfaces studied by UHV reflection electron microscopy," *Ultramicroscopy* **29**(1), 161–167 (1989).
- ⁸P. S. Ho, "Motion of inclusion induced by a direct current and a temperature gradient," *J. Appl. Phys.* **41**(1), 64–68 (1970).
- ⁹A. Mukherjee, R. Mukherjee, K. Ankit, A. Bhattacharya, and B. Nestler, "Influence of substrate interaction and confinement on electric-field-induced transition in symmetric block-copolymer thin films," *Phys. Rev. E* **93**, 032504 (2016).
- ¹⁰A. Mukherjee, K. Ankit, A. Reiter, M. Selzer, and B. Nestler, "Electric-field-induced lamellar to hexagonally perforated lamellar transition in diblock copolymer thin films: Kinetic pathways," *Phys. Chem. Chem. Phys.* **18**(36), 25609–25620 (2016).
- ¹¹M. D. Morariu, N. E. Voicu, E. Schäffer, Z. Lin, T. P. Russell, and U. Steiner, "Hierarchical structure formation and pattern replication induced by an electric field," *Nat. Mater.* **2**(1), 48 (2003).
- ¹²I. Dutta and P. Kumar, "Electric current induced liquid metal flow: Application to coating of micropatterned structures," *Appl. Phys. Lett.* **94**(18), 184104 (2009).
- ¹³D. Du and D. Srolovitz, "Electrostatic field-induced surface instability," *Appl. Phys. Lett.* **85**(21), 4917–4919 (2004).
- ¹⁴I. A. Blech, "Electromigration in thin aluminum films on titanium nitride," *J. Appl. Phys.* **47**(4), 1203–1208 (1976).
- ¹⁵G. Posser, V. Mishra, R. Reis, and S. S. Sapatnekar, "Analyzing the electromigration effects on different metal layers and different wire lengths," in *2014 21st IEEE International Conference on Electronics, Circuits and Systems (ICECS)* (IEEE, 2014), pp. 682–685.
- ¹⁶Q. Ma and Z. Suo, "Precipitate drifting and coarsening caused by electromigration," *J. Appl. Phys.* **74**(9), 5457–5462 (1993).
- ¹⁷C. Witt, C. Volkert, and E. Arzt, "Electromigration-induced Cu motion and precipitation in bamboo Al-Cu interconnects," *Acta Mater.* **51**(1), 49–60 (2003).
- ¹⁸R. Yongsunthorn, C. Tao, P. Rous, and E. Williams, "Surface electromigration and current crowding," in *Nanophenomena at Surfaces* (Springer, 2011), pp. 113–143.
- ¹⁹J.-J. Métois and M. Audiffren, "An experimental study of step dynamics under the influence of electromigration: Si(111)," *Int. J. Mod. Phys. B* **11**(31), 3691–3702 (1997).
- ²⁰W. Wang, Z. Suo, and T.-H. Hao, "A simulation of electromigration-induced transgranular slits," *J. Appl. Phys.* **79**(5), 2394–2403 (1996).
- ²¹M. Schimschak and J. Krug, "Electromigration-induced breakup of two-dimensional voids," *Phys. Rev. Lett.* **80**, 1674–1677 (1998).
- ²²T.-H. Hao and Q.-M. Li, "Linear analysis of electromigration-induced void instability in Al-based interconnects," *J. Appl. Phys.* **83**(2), 754–759 (1998).
- ²³Y. Li, Z. Li, X. Wang, and J. Sun, "Analytical solution for motion of an elliptical inclusion in gradient stress field," *J. Mech. Phys. Solids* **58**(7), 1001–1010 (2010).
- ²⁴H. Mehl, O. Biham, O. Millo, and M. Karimi, "Electromigration-induced flow of islands and voids on the Cu (001) surface," *Phys. Rev. B* **61**(7), 4975 (2000).
- ²⁵O. Pierre-Louis and T. Einstein, "Electromigration of single-layer clusters," *Phys. Rev. B* **62**(20), 13697 (2000).
- ²⁶P. Kuhn, J. Krug, F. Hausser, and A. Voigt, "Complex shape evolution of electromigration-driven single-layer islands," *Phys. Rev. Lett.* **94**(16), 166105 (2005).
- ²⁷D. Dasgupta and D. Maroudas, "Surface nanopatterning from current-driven assembly of single-layer epitaxial islands," *Appl. Phys. Lett.* **103**(18), 181602 (2013).
- ²⁸A. Kumar, D. Dasgupta, and D. Maroudas, "Surface nanopattern formation due to current-induced homoepitaxial nanowire edge instability," *Appl. Phys. Lett.* **109**(11), 113106 (2016).
- ²⁹D. Dasgupta, A. Kumar, and D. Maroudas, "Analysis of current-driven oscillatory dynamics of single-layer homoepitaxial islands on crystalline conducting substrates," *Surf. Sci.* **669**, 25–33 (2018).
- ³⁰J. Cho, M. Rauf Gungor, and D. Maroudas, "Current-driven interactions between voids in metallic interconnect lines and their effects on line electrical resistance," *Appl. Phys. Lett.* **88**(22), 221905 (2006).
- ³¹M. Schimschak and J. Krug, "Electromigration-driven shape evolution of two-dimensional voids," *J. Appl. Phys.* **87**(2), 695–703 (2000).
- ³²M. R. Gungor and D. Maroudas, "Electromigration-induced failure of metallic thin films due to transgranular void propagation," *Appl. Phys. Lett.* **72**(26), 3452–3454 (1998).
- ³³Z. Suo, W. Wang, and M. Yang, "Electromigration instability: Transgranular slits in interconnects," *Appl. Phys. Lett.* **64**(15), 1944–1946 (1994).
- ³⁴J. Santoki, A. Mukherjee, D. Schneider, M. Selzer, and B. Nestler, "Phase-field study of electromigration-induced shape evolution of a transgranular finger-like slit," *J. Electron. Mater.* **48**(1), 182–193 (2019).
- ³⁵D. Dasgupta, G. I. Sfyris, and D. Maroudas, "Current-driven morphological evolution of single-layer epitaxial islands on crystalline substrates," *Surf. Sci.* **618**, L1–L5 (2013).
- ³⁶M. Wilms, J. Conrad, K. Vasilev, M. Kreiter, and G. Wegner, "Manipulation and conductivity measurements of gold nanowires," *Appl. Surf. Sci.* **238**(1–4), 490–494 (2004).
- ³⁷A. Kumar, D. Dasgupta, C. Dimitrakopoulos, and D. Maroudas, "Current-driven nanowire formation on surfaces of crystalline conducting substrates," *Appl. Phys. Lett.* **108**(19), 193109 (2016).
- ³⁸Z. J. Morgan and Y. M. Jin, "Phase field modeling of pore electromigration in anisotropic conducting polycrystals," *Comput. Mater. Sci.* **172**, 109362 (2020).
- ³⁹Y. Li, X. Wang, and Z. Li, "The morphological evolution and migration of inclusions in thin-film interconnects under electric loading," *Compos. Part B* **43**(3), 1213–1217 (2012).
- ⁴⁰J. Santoki, A. Mukherjee, D. Schneider, and B. Nestler, "Role of conductivity on the electromigration-induced morphological evolution of inclusions in {110}-oriented single crystal metallic thin films," *J. Appl. Phys.* **126**(16), 165305 (2019).
- ⁴¹F. Haußer, S. Rasche, and A. Voigt, "The influence of electric fields on nanostructures-simulation and control," *Math. Comput. Simul.* **80**(7), 1449–1457 (2010).
- ⁴²L. Bañas and R. Nürnberg, "Phase field computations for surface diffusion and void electromigration in \mathbb{R}^3 ," *Comput. Visual. Sci.* **12**(7), 319–327 (2009).
- ⁴³D. N. Bhatte, A. Kumar, and A. F. Bower, "Diffuse interface model for electromigration and stress voiding," *J. Appl. Phys.* **87**(4), 1712–1721 (2000).
- ⁴⁴M. Mahadevan and R. M. Bradley, "Simulations and theory of electromigration-induced slit formation in unpassivated single-crystal metal lines," *Phys. Rev. B* **59**, 11037–11046 (1999).
- ⁴⁵W. Farmer and K. Ankit, "Phase-field simulations of electromigration-induced defects in interconnects with non-columnar grain microstructure," *J. Appl. Phys.* **127**(17), 175301 (2020).
- ⁴⁶A. Ishii and A. Yamanaka, "Multi-phase-field modelling of electromigration-induced void migration in interconnect lines having bamboo structures," *Comput. Mater. Sci.* **184**, 109848 (2020).
- ⁴⁷S. S. Vemulapalli, "Phase-field modeling of electromigration-mediated morphological evolution of voids in interconnects," Ph.D. thesis (Arizona State University, 2020).
- ⁴⁸J. W. Barrett, H. Garcke, and R. Nürnberg, "A phase field model for the electromigration of intergranular voids," *Interfaces Free Bound.* **9**(2), 171–210 (2007).
- ⁴⁹V. Attari, S. Ghosh, T. Duong, and R. Arroyave, "On the interfacial phase growth and vacancy evolution during accelerated electromigration in Cu/Sn/Cu microjoints," *Acta Mater.* **160**, 185–198 (2018).
- ⁵⁰A. Mukherjee, K. Ankit, R. Mukherjee, and B. Nestler, "Phase-field modeling of grain-boundary grooving under electromigration," *J. Electron. Mater.* **45**(12), 6233–6246 (2016).
- ⁵¹A. Mukherjee, K. Ankit, M. Selzer, and B. Nestler, "Electromigration-induced surface drift and slit propagation in polycrystalline interconnects: Insights from phase-field simulations," *Phys. Rev. Appl.* **9**, 044004 (2018).
- ⁵²A. Mukherjee, "Electric field-induced directed assembly of diblock copolymers and grain boundary grooving in metal interconnects," Ph.D. thesis (Karlsruher Institut für Technologie, 2019).

- ⁵³S. Pfeifer, S. Großmann, R. Freudenberger, H. Willing, and H. Kappl, "Characterization of intermetallic compounds in Al-Cu-bimetallic interfaces," in *2012 IEEE 58th Holm Conference on Electrical Contacts (Holm)* (IEEE, 2012), pp. 1–6.
- ⁵⁴L. Zhang, S. Ou, J. Huang, K.-N. Tu, S. Gee, and L. Nguyen, "Effect of current crowding on void propagation at the interface between intermetallic compound and solder in flip chip solder joints," *Appl. Phys. Lett.* **88**(1), 012106 (2006).
- ⁵⁵Y. Yao, Y. Wang, L. M. Keer, and M. E. Fine, "An analytical method to predict electromigration-induced finger-shaped void growth in snagcu solder interconnect," *Scr. Mater.* **95**, 7–10 (2015).
- ⁵⁶A. Latz, S. Sindermann, L. Brendel, G. Dumpich, F. M. zu Heringdorf, and D. Wolf, "Anisotropy of electromigration-induced void and island drift," *J. Phys. Condens. Matter* **26**(5), 055005 (2013).
- ⁵⁷O. Kraft and E. Arzt, "Electromigration mechanisms in conductor lines: Void shape changes and slit-like failure," *Acta Mater.* **45**(4), 1599–1611 (1997).
- ⁵⁸M. R. Gungor and D. Maroudas, "Theoretical analysis of electromigration-induced failure of metallic thin films due to transgranular void propagation," *J. Appl. Phys.* **85**(4), 2233–2246 (1999).
- ⁵⁹J. Krug and H. T. Dobbs, "Current-induced faceting of crystal surfaces," *Phys. Rev. Lett.* **73**, 1947–1950 (1994).
- ⁶⁰D. Maroudas, "Dynamics of transgranular voids in metallic thin films under electromigration conditions," *Appl. Phys. Lett.* **67**(6), 798–800 (1995).
- ⁶¹C.-Y. Li, P. Børgesen, and T. Sullivan, "Stress-migration related electromigration damage mechanism in passivated, narrow interconnects," *Appl. Phys. Lett.* **59**(12), 1464–1466 (1991).
- ⁶²J. Prybyla, S. Riege, S. Grabowski, and A. Hunt, "Temperature dependence of electromigration dynamics in al interconnects by real-time microscopy," *Appl. Phys. Lett.* **73**(8), 1083–1085 (1998).
- ⁶³P. Goli, H. Ning, X. Li, C. Y. Lu, K. S. Novoselov, and A. A. Balandin, "Thermal properties of graphene–copper–graphene heterogeneous films," *Nano Lett.* **14**(3), 1497–1503 (2014).
- ⁶⁴K. Mohsin, A. Srivastava, A. Sharma, C. Mayberry, and M. Fahad, "Temperature sensitivity of electrical resistivity of graphene/copper hybrid nano ribbon interconnect: A first principle study," *ECS J. Solid State Sci. Technol.* **6**(4), P119–P124 (2017).
- ⁶⁵E. Arzt, O. Kraft, W. D. Nix, and J. E. Sanchez, "Electromigration failure by shape change of voids in bamboo lines," *J. Appl. Phys.* **76**(3), 1563–1571 (1994).